Afterbody Flow Fields and Skin Friction on Short Duct Fan Nacelles

ROBERT L. LAWRENCE*
The Boeing Company, Renton, Wash.

Afterbody skin friction is a major component of short duct turbofan engine nacelle drag. Experimental measurements of afterbody skin-friction drag and flow fields on models with short duct geometries are presented for freestream Mach numbers zero and eight-tenths. Boundary-layer theory is used with the velocity decay measurements in an attempt to predict the skin-friction drag. For fan nozzle pressure ratios less than 2.8, there is satisfactory agreement between predicted and measured drag; however, predicted drag is lower than measured drag at pressure ratios greater than 2.8. When the freestream Mach number is zero, velocity profiles are found which are identical to Glauert's incompressible wall jet profile; at Mach 0.8, profiles similar but not identical to Glauert's profile are found for some test conditions. The velocity decay downstream of the core is described by $U_M/U_F = K(X/h)^B$ (for Mach 0) and $(U_M - U_\infty)/(U_F - U_\infty) = K(X/h)^B$ (for Mach 0.8), where U is velocity, X equals distance along afterbody, h is the height of the fan opening, ∞ means freestream, and K and B are empirical functions of fan nozzle pressure ratio.

Nomenclature

A/A^* = area ratio corresponding to M_F for convergent supercritical nozzles
A_F = fan nozzle exit area
A_w = nacelle afterbody wetted area
B = constant in Eq. (4)
C_f = afterbody mean skin-friction coefficient $C_f = D/(\rho_F U_F^2 A_w/2)$
D = skin-friction drag
Fg = fan gross thrust [Eq. (3)]
h = fan exit height
K = constant in Eq. (4)
L = afterbody length
M = Mach number
P = pressure
q = $\frac{1}{2}\rho U^2 = \frac{1}{2}\gamma P M^2$
r = radial distance outward from the afterbody surface
R_F = Reynolds number, $R_F = U_F L/\nu_F$
R = gas constant for air
R_1 = afterbody radius, $R_1 = 1.5$ in. for the models
T = temperature
U = velocity
X = distance downstream from fan nozzle exit
γ = ratio of specific heats, $\gamma = 1.4$
ρ = density
ϕ = velocity parameter, $\phi = (U_M - U_\infty)/(U_F - U_\infty)$ when $M_\infty = 0.8$
δ_2 = value of r at $U = U_M/2$ for $M_\infty = 0$; value of r at $U = (U_M + U_\infty)/2$ for $M_\infty = 0.8$
δ = $P_\infty \div$ standard atmospheric pressure
$\delta(X)$ = boundary-layer thickness along afterbody
δ_M = value of r at $U = U_M$
δ_c = boundary-layer thickness at $(X/h)_c$
$\tau_w(X)$ = shear stress along afterbody surface
ν = kinematic viscosity
θ = boundary-layer momentum thickness

$$\theta = \theta(X) = \int_0^{\delta_M} \frac{U}{U_M}\left(1 - \frac{U}{U_M}\right) dr$$

Subscripts

c = at the downstream end of the core region
F = fan nozzle exit or jet, fully expanded
i = indicated pressure by a probe on the total pressure rake
M = at the point of maximum velocity in the profile at a given X
MIN = minimum static pressure on the afterbody
t = stagnation conditions
∞ = freestream

Superscript

$*$ = sonic, at the convergent fan nozzle exit where $M = 1$

Presented as Preprint 64-609 at the AIAA Transport Aircraft Design and Operations Meeting, Seattle, Wash., August 10–12, 1964; revision received December 4, 1964.

* Research Engineer. Member AIAA.

I. Introduction

AIRCRAFT manufacturers must continually evaluate airframe-engine combinations as part of the task of offering optimum aircraft for a prescribed mission. When front-fan turbofan engines are considered, the selection of a long or short duct turbofan engine (Fig. 1) for a particular application is dictated by weight, performance, thrust minus drag, and engine-airframe compatibility. Nacelle drag (including interference drag and nacelle afterbody drag) contributes about 8% of total airplane drag for a good Mach 0.8 transport design. For the short duct turbofan installation, the afterbody drag approaches 50% of the nacelle drag, or 4% of the total airplane drag.

The Boeing Company has conducted a series of model tests to measure the scrubbing drag that occurs on the afterbody of short duct nacelles. In addition, measurements were made in

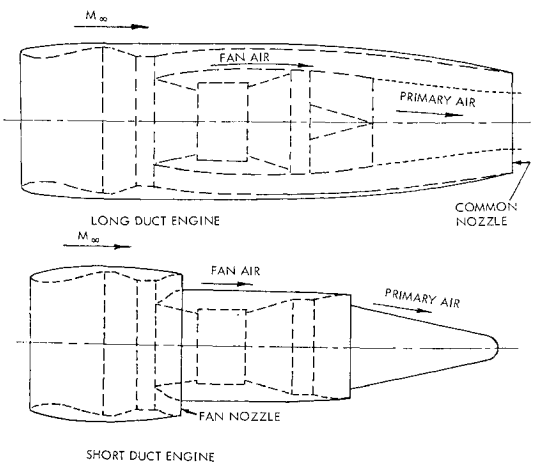

Fig. 1 Long and short duct engines.

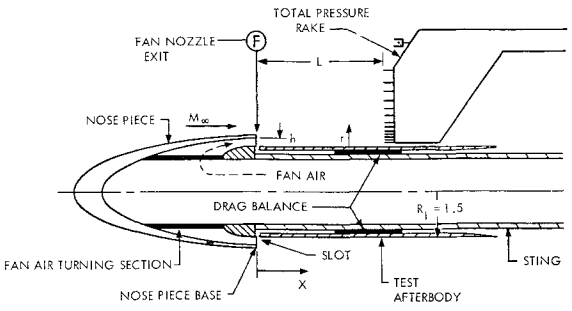

Fig. 2 Model to simulate fan nozzle annulus.

the flow field on the afterbody in order to gain insight into the flow conditions that influence the drag. The tests were divided into two parts: an investigation of the flow field, and the measurement of the skin-friction drag on cylindrical afterbodies. Geometries and flow conditions were chosen to simulate a wide range of bypass ratios consistent with expected commercial use. The experiments provide important information, which can be used in deciding whether to use long or short duct turbofan engines for a given mission.

II. Experimental Apparatus

In order to separate the skin-friction drag from other effects, a cylindrical afterbody model was chosen. A convergent annular fan opening was simulated as shown in Fig. 2. The drag balance measured all axial forces on the afterbody, which was isolated from the rest of the apparatus by a small annular slot at the forward edge. The afterbody base was beveled to a point to create a constant-pressure region on the base. The indicated drag balance force was corrected by the pressure forces in the slot and on the afterbody base, so that the skin-friction drag on the surface of the afterbody could be isolated. A total-pressure rake was constructed to measure radial velocity profiles at the fan nozzle exit and at several stations along the afterbody.

To minimize the external boundary layer, it was necessary to keep the nosepiece as short as possible and avoid supervelocity effects, which might induce local shocks or separation. Accordingly, the surface was chosen to be an ellipsoid of revolution, designed to avoid local shocks.[2] A separate combination of nosepiece and turning section was used for each simulated fan height (Fig. 3). Figure 4 shows the boundary layer on the trailing edges of three nosepieces due to freestream flow at $M_\infty = 0.8$. The tests were run in a 20-in. free-jet tunnel. The air to simulate the fan flow was brought forward through a sting and turned 180° through a fan air turning section.

III. Pressure Measurements

Definitions

True velocity measurements were not made. The velocity was calculated from the indicated total pressures referred to as

Table 1 Test conditions for pressure measurements

Fan heights, in.	Afterbody axial positions, in.	Fan nozzle exit pressure ratios	Freestream Mach number
0.09	0	2	0
0.18	3	2.8	0.8
0.27	6	3.6	...
0.36	9	4.4	...
0.45	12	...	...

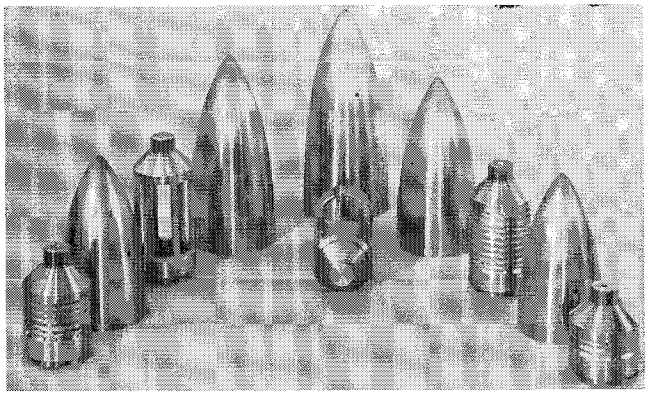

Fig. 3 Nosepieces and fan air turning sections.

tunnel static pressure:

$$U = M(\gamma g R T)^{1/2} \tag{1}$$

where

$$T = T_t/[1 + M^2(\gamma - 1)/2]$$

$$M = [(P/P_{ti})^{-(\gamma-1)/\gamma} - 1]^{1/2}[2/(\gamma - 1)]^{1/2}$$

and T_t was assumed constant throughout the boundary layer. The fan nozzle exit pressure ratio was defined by a momentum-averaged integration of the total-pressure profile:

$$P_{tF} = \frac{\int_{R_1}^{h+R_1} P_{ti}(\rho^* U^* U_F) 2\pi(R_1 + r)dr}{\int_{R_1}^{h+R_1} (\rho^* U^* U_F) 2\pi(R_1 + r)dr} \tag{2}$$

The denominator is the fully expanded or isentropic fan momentum, and it is called the fan gross thrust:

$$Fg = \int_{R_1}^{h+R_1} (\rho U^* U^*_F) 2\pi(R_1 + r)dr \tag{3}$$

Test Conditions

Measurements were made at five fan heights, four pressure ratios, and five axial locations. Table 1 gives the scope of the test conditions. Each fan height was run with every combination of axial position, freestream Mach number, and pressure ratio, making 200 test conditions in all.

Louvered fan air turning sections (Fig. 3) were designed to provide a uniform velocity field at the fan nozzle exit. However, it was discovered that slightly better profiles were

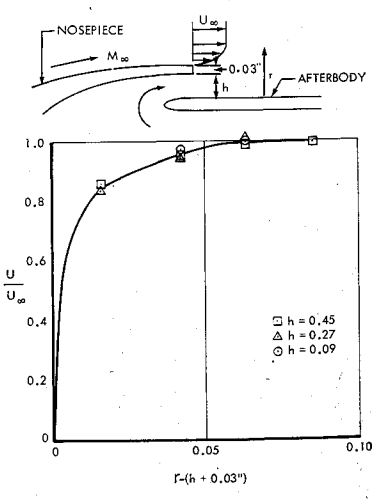

Fig. 4 Boundary layer on outer surface of nosepiece trailing edges.

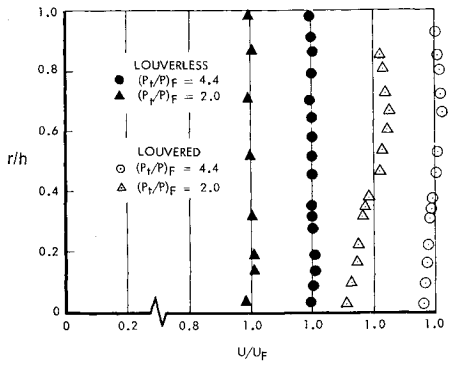

Fig. 5 Fan nozzle exit velocity profiles: $X = 0$, $M_\infty = h = 0.45$, convergent nozzles.

measured in turning sections with the louvers removed as shown in Fig. 5.

IV. Flow Field on Afterbody at $M_\infty = 0$

Velocity Decay

The fan nozzle annulus has the geometry of an axisymmetric wall jet. As a measure of the decrease of the jet velocities, the decay of the maximum velocity is observed as a function of the number of fan heights X/h downstream from the fan exit. At each value of X/h, a velocity profile $U(r)$ will exist with a maximum velocity U_M. In a wall jet, U_M/U_F is 1.0 from the jet exit to a position some distance downstream, called the "core" length $(X/h)_c$. At $(X/h)_c$, the mixing region extends to all parts of the velocity profile, and U_M/U_F starts decreasing. For the plane incompressible wall jet, the rate of decay of the maximum velocity is given by

$$U_M/U_F = K(X/h)^B = 3.45(X/h)^{-0.5} \quad (4)$$

Equation (4) plotted on log paper is a straight line of slope B, intersecting the line $U_M/U_F = 1$ at $(X/h)_c$. The compressible axially symmetric wall jet data were plotted similarly in Fig. 6. At each pressure ratio, the data may be represented by a straight line intersecting $U_M/U_F = 1$ at a value of X/h which will be called $(X/h)_c$; furthermore, each line has the same slope, $B = -0.41$. Thus, for $M_\infty = 0$, K is a function of $(P_t/P)_F$, and B is -0.41. This value of B differs from the incompressible plane wall jet, probably as a result of axial symmetry; it may be that B would be -0.5 for a plane compressible wall jet.

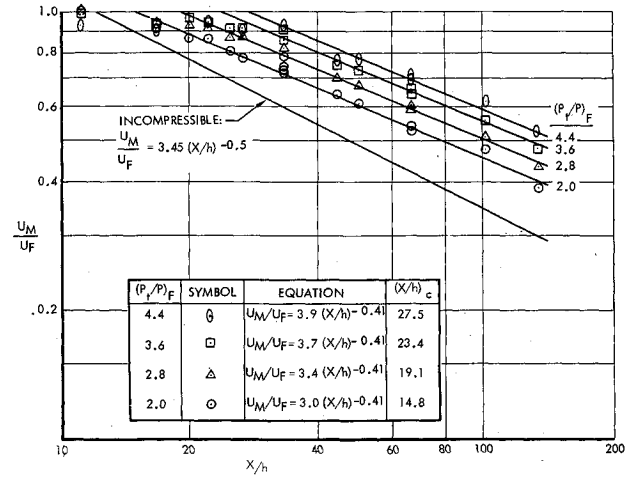

Fig. 6 Velocity decay: $M_\infty = 0$, louvered turning sections, convergent nozzles.

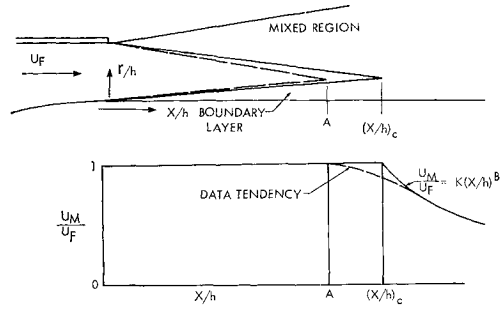

Fig. 7 Core length definition.

Core Region

Figure 7 shows the defined core length $(X/h)_c$. From the fan exit to $(X/h)_c$, U_M/U_F is 1.0. However, the measured U_M/U_F is below 1.0 at the defined value of $(X/h)_c$ (Fig. 6) and reaches 1.0 at some point A that is smaller than $(X/h)_c$. This is caused by boundary layers and core region shocks. Boundary layers exist on both the inner and outer surfaces of the fan nozzle; the total pressure in these boundary layers is less than fan exit total pressure. The wake caused by the nosepiece trailing edge feeds into the mixing region. Shocks exist in the core region, and these lower the total-pressure readings. When the probes are in supersonic flow regions, normal shocks in front of the probes lower the indicated total-pressure readings. It is impossible to tell which combination of the preceding factors influence a given total-pressure reading in the core region, but it is important to recognize that such factors exist, and all tend to lower the indicated readings.

The complex nature of the core region flow is shown in a shadowgraph (Fig. 8). Although distortion (caused by three-dimensional effects) is present, the shock and expansion patterns are visible. Figure 9 is a sketch of the flow in Fig. 8. The flow leaves the convergent fan nozzle at the Mach number $M^* = 1.0$. At the nosepiece trailing edge, the flow undergoes a Prandtl-Meyer expansion to the free-stream pressure P_∞, yielding the fully expanded fan exit velocity M_F. Expansion waves emanating from the corner are reflected as expansion waves from the boundary layer causing the static pressure to drop to a minimum value well below P_∞; the value of P_{MIN} depends on $(P_t/P)_F$. For example, when $(P_t/P)_F = 4.4$ (Ref. 10), M_F would be 1.62, and the Mach number corresponding to P_{MIN} would be near 2.0. The expansion waves reflected from the boundary layer are reflected from the mixing region as compression waves, which are in turn reflected as compression waves from the boundary layer, converging to form the first shock wave. Similar patterns are repeated downstream until the flow becomes subsonic. The static pressure decreases from P^* at the end of the convergent nozzle to P_{MIN} and then increases continuously until the point where the shock is encountered, where a discontinuous jump occurs. The total pressure remains constant until a shock is encountered, where a sudden small decrease in total pressure occurs. The pressure pattern, like the shock pattern, will repeat itself until the static pressure equals P_∞.

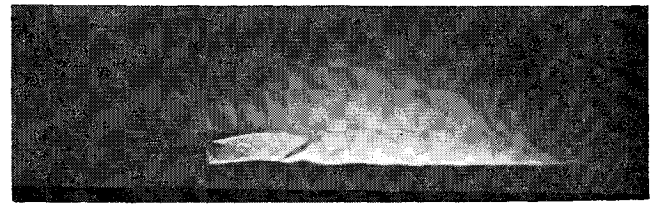

Fig. 8 Core region shadowgraph: $h = 0.27$, $M_\infty = 0$, $(P_t/P)_F = 3.6$.

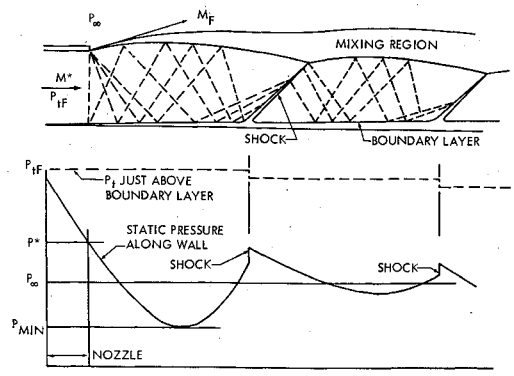

Fig. 9 Core region.

Louverless Turning Sections

For model fan heights of 0.36 and 0.45 in., pressure surveys were made for flows produced by turning sections that had the louvered vanes removed. The runs with louverless turning sections were limited to runs where $(X/h) < 33$. Consequently, data were not sufficient to establish the slope B in a log plot of U_M/U_F vs X/h. It was assumed, therefore, that the slope B would be the same as for the louvered turning sections. Figure 10 shows the louverless data for $M_\infty = 0$. The lines were drawn parallel to each other with a slope of -0.41, and the points at larger X/h were weighed more heavily. The effect of removing the louvers was to shift the curves toward lower $(X/h)_c$. The differences may be related to changes in turbulence level caused by removing the louvers. Care should be exercised when using the data to estimate core lengths for other internal nozzle geometries.

Velocity Profiles[1]

Definitions

The value of U will be zero on the surface of the afterbody where $r = 0$; it will rise to a maximum value U_M and then fall to zero as r grows large. The term δ_M is the value of r at U_M. The velocity $U_M/2$ will be reached in two locations. The term δ_2 is defined as the value of r where $U = U_M/2$, and $r > \delta_M$.

Velocity profiles downstream of the core at $M_\infty = 0$

A theoretical analysis by Glauert[3] indicates that a plane two-dimensional, incompressible wall jet has "similar" velocity profiles, which are independent of X, when the profiles are plotted U/U_M vs r/δ_2. The profiles of the experiment are

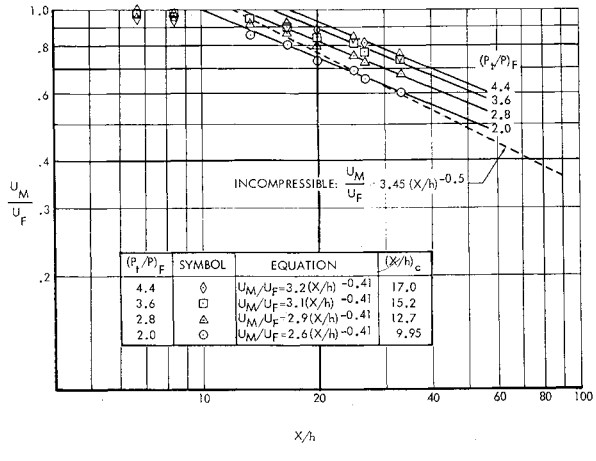

Fig. 10 Velocity decay: $M_\infty = 0$, louverless turning sections, convergent nozzles.

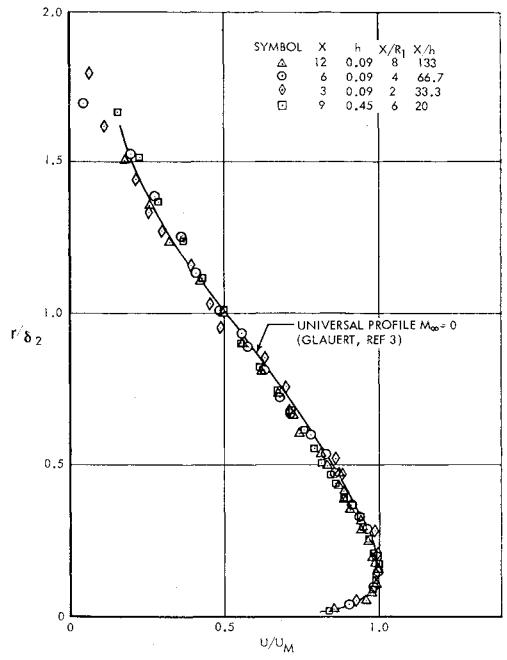

Fig. 11 Axisymmetric compressible wall jet velocity profile: $M_\infty = 0$, $(P_t/P)_F = 2.0$, louvered turning sections, convergent nozzles.

plotted using these parameters. Figures 11 and 12 show profiles for $M_\infty = 0$ and fan exit pressure ratios of 2.0 and 4.4, respectively. The range of X/R_1 changes by a factor of 4. All data of these figures closely follow Glauert's universal profile for plane incompressible wall jet flow.[3] As a result, the following conclusions are made for a compressible wall jet from a convergent nozzle: When (X/h) is greater than $(X/h)_c$, the compressible wall jet velocity profiles are similar to each other and are identical to Glauert's incompressible universal profile up to a pressure ratio of 4.4; within the range $2 < X/R_1 < 8$, no significant axisymmetric effect on velocity profiles is found.

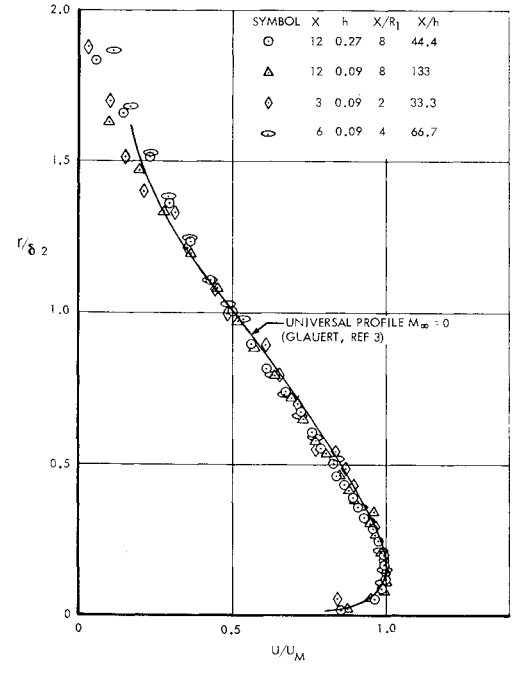

Fig. 12 Axisymmetric compressible wall jet velocity profiles: $M_\infty = 0$, $(P_t/P)_F = 4.4$, louvered turning sections, convergent nozzles.

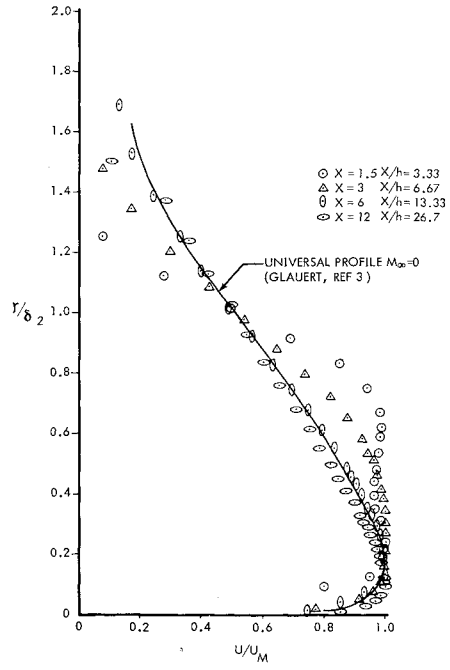

Fig. 13 Axisymmetric compressible wall jet velocity profiles in the core region: $M_\infty = 0$, $h = 0.45$, $(P_t/P)_F = 4.4$, louverless turning sections, convergent nozzles.

Velocity profiles in the core region

When the flow leaves the fan exit, the velocity profiles are uniform (Fig. 5). As the flow proceeds downstream from the fan exit, the profile changes from a "square" profile at the exit to a Glauert profile near $(X/h)_c$. Figure 13 shows this process for louverless turning sections at a fan exit pressure ratio of 4.4.

Jet Spreading

The manner in which a wall jet spreads is described by a plot of the position δ_2 of the half velocity as a function of the distance X downstream from the fan exit. The coordinates are nondimensionalized by the fan height h (Fig. 14). Although there is scatter in these plots, it is evident that the jet

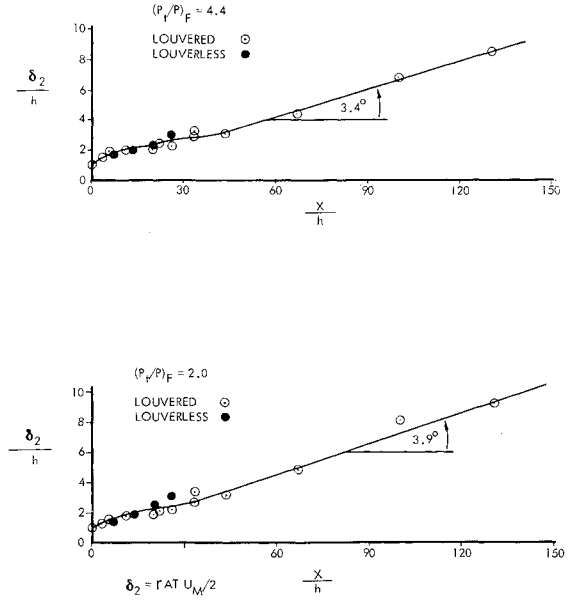

Fig. 14 Axisymmetric compressible wall jet spreading: $M_\infty = 0$, $(P_t/P)_F = 2.0$ and 4.4, convergent nozzles.

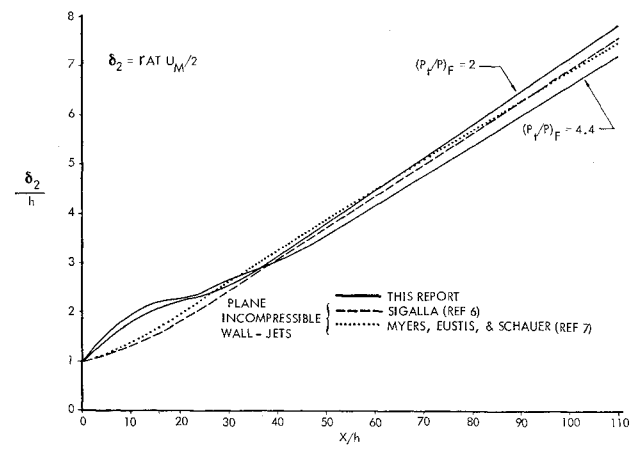

Fig. 15 Compressible wall jet spreading compared to incompressible data: $M_\infty = 0$, convergent nozzles.

flow at the fan exit comes out at a relatively steep angle, and the angle for a pressure ratio of 4.4 is larger than for 2.0. After the initial outward thrust, the jet expands along a straight line of about $3\frac{1}{2}°$. The lines drawn in Fig. 14 are shown for 3.4° and 3.9°, but the accuracy is probably $\pm\frac{1}{2}°$. In Fig. 15, the compressible jet spreading found in this experiment is compared with previous work[6–8] on incompressible, plane wall jets. Beyond $X/h = 30$, the jets spread similarly, but in the region near the fan exit the compressible jet spreads more rapidly. It is concluded that the spreading of an underexpanded compressible wall jet as measured by δ_2 is initially more rapid than for an incompressible wall jet; when $X/h > 30$, the spreading is similar to the spreading of an incompressible wall jet.

V. Flow Field on Afterbody at $M_\infty = 0.8$

Velocity Decay

When two flow regions exist side by side, the mixing ought to be strongly influenced by the velocity difference between the two adjacent flows. When M_∞ is zero, the velocity difference is $(U_M - 0) = U_M$. When $M_\infty = 0.8$, the velocity difference is $(U_M - U_\infty)$. Therefore, for the case where $M_\infty = 0.8$, U_M/U_F is replaced by $\phi = (U_M - U_\infty)/(U_F - U_\infty)$. The data are shown on plots of ϕ vs X/h on log paper. The velocity decay shown in Fig. 16 represents the decay of the velocity difference between the jet and the freestream air for a louvered turning section. The data can no longer be represented by a series of parallel lines, each representing a fan exit pressure ratio. However, each pressure ratio may be

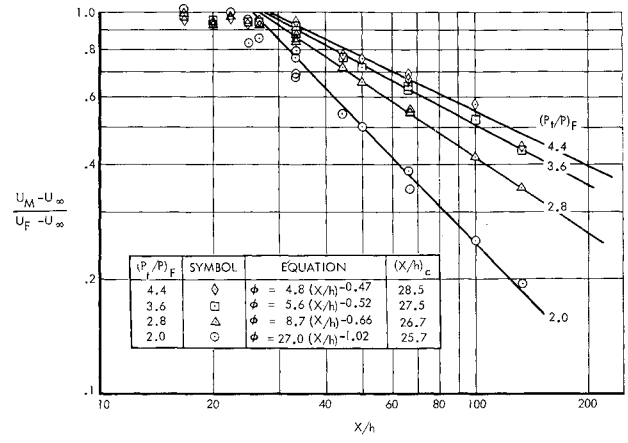

Fig. 16 Velocity decay: $M_\infty = 0.8$, louvered turning sections, convergent nozzles.

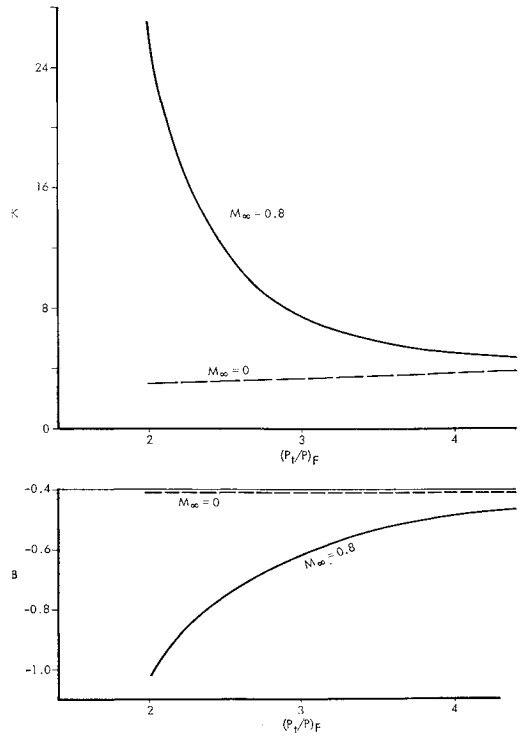

Fig. 17 Correlation equations constants, $M_\infty = 0$ and $M_\infty = 0.8$, compared: louvered turning sections.

represented by a straight line, with the same divergence from the data near $(X/h)_c$ as occurred for $M_\infty = 0$. Thus, each pressure ratio is represented by an equation similar in form to Eq. (4):

$$\phi = K(X/h)^B = (U_M - U_\infty)/(U_F - U_\infty) \qquad (5)$$

In this case, however, both K and B are functions of the fan exit pressure ratio. Figure 17 compares K and B for the louvered nosepieces at $M_\infty = 0$ and $M_\infty = 0.8$. As $(P_t/P)_F$ gets larger, the values of K and B for $M_\infty = 0.8$ approach the values of K and B for $M_\infty = 0$. At large $(P_t/P)_F$, the quantity $(U_M - U_\infty)/(U_F - U_\infty)$ approaches U_M/U_F, since U_∞ becomes small relative to U_M and U_F. The wall jet characteristics where $M_\infty > 0$ should be similar to those at $M_\infty = 0$ when $U_F \gg U_\infty$.

Core Region

The previous discussion of the core region for $M_\infty = 0$ applies equally well for $M_\infty = 0.8$. Figure 18 is a shadowgraph of the core region for $M_\infty = 0.8$; it may be compared with Fig. 8, which is at the same pressure ratio, 3.6. Figure 18 shows more clearly the jet mixing boundaries.

Louverless Turning Sections

Limited data are available for louverless turning sections at $M_\infty = 0.8$. Again, it was decided to draw lines through

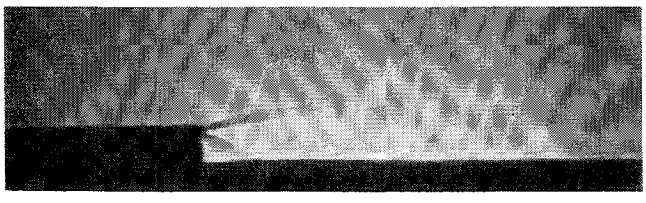

Fig. 18 Core region shadowgraph: $M_\infty = 0.8$, $h = 0.36$, $(P_t/P)_F = 3.6$.

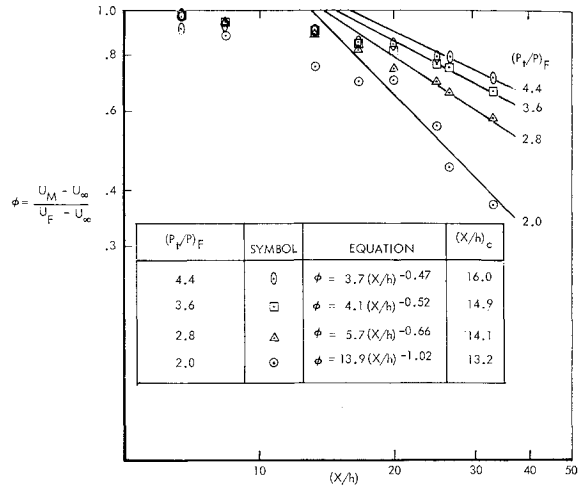

Fig. 19 Velocity decay: $M_\infty = 0.8$, louverless turning sections, convergent nozzles.

the data with slopes parallel to the louvered lines for the same pressure ratios. Figure 19 is the result.

Velocity Profiles

Definitions

When $U_\infty > 0$, the velocity profile is plotted in terms of $(U - U_\infty)$, which begins at $-U_\infty$ where $U = 0$ at the wall. It rises through zero $(U = U_\infty)$ to a maximum value $(U_M - U_\infty)$ and then decreases approaching zero at large r. At some point for r greater than δ_M, a point is reached where $U = (U_M + U_\infty)/2$, and the corresponding value of r is δ_2. The coordinates are nondimensionalized by δ_2 and $(U_M - U_\infty)$.

Velocity profiles downstream of the core at $M_\infty = 0.8$

The velocity profiles downstream from the core are shown for a fan exit pressure ratio of 4.4 in Fig. 20. The profiles fall on one curve, establishing that the profiles are similar and fall

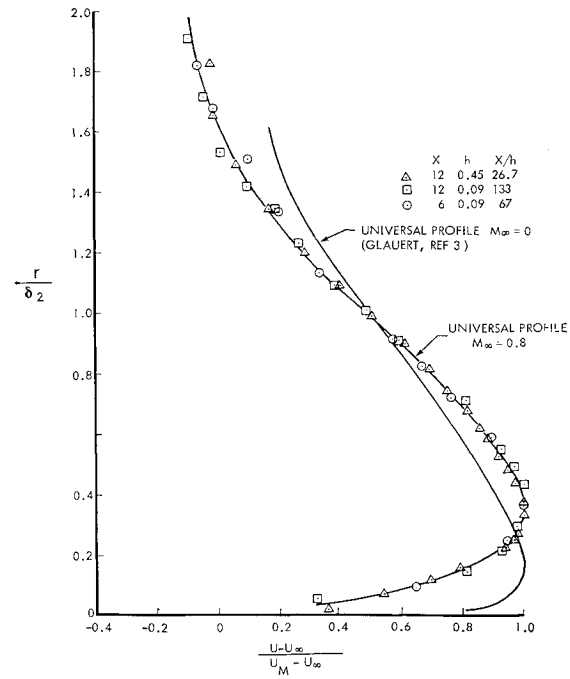

Fig. 20 Axisymmetric compressible wall jet velocity profiles: $M_\infty = 0.8$, $(P_t/P)_F = 4.4$, louvered turning sections, convergent nozzles.

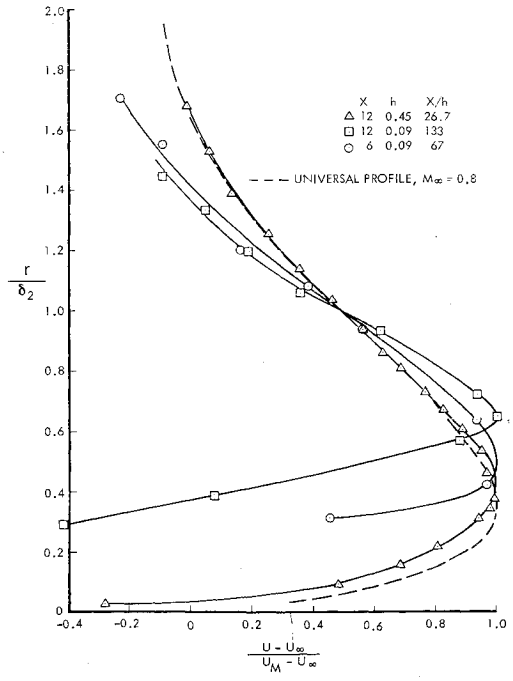

Fig. 21 Axisymmetric compressible wall jet velocity profiles: $M_\infty = 0.8$, $(P_t/P)_F = 2.0$, louvered turning sections, convergent nozzles.

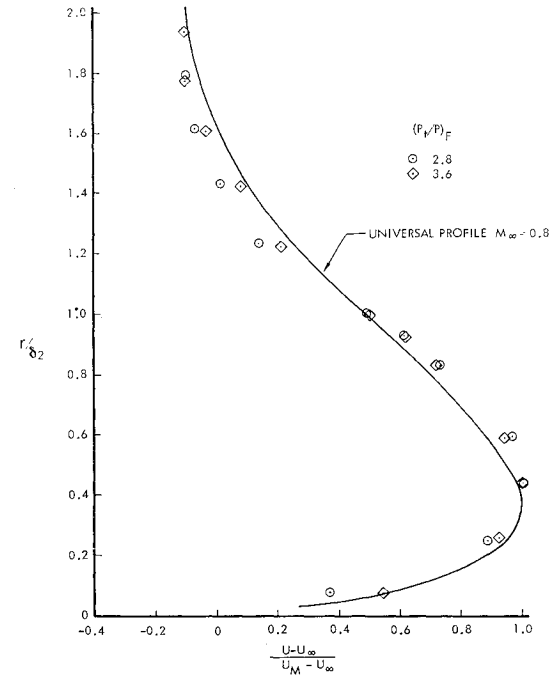

Fig. 23 Axisymmetric compressible wall jet velocity profiles: $M_\infty = 0.8$, $X/h = 66.7$, louvered turning sections, convergent nozzles.

on a universal profile. Figure 20 also shows Glauert's universal profile for $M_\infty = 0$, and δ_M is greater for the $M_\infty = 0.8$ profiles than for the $M_\infty = 0$ profiles. The universality of profiles does not extend to the case where $(P_t/P)_F = 2.0$ and $M_\infty = 0.8$. Figure 21 shows that, at each value of X/h, the velocity profile differs, and all profiles have a greater δ_M than for the profile at $(P_t/P)_F = 4.4$. This happens because the velocity difference no longer predominates as the major factor in the boundary-layer formation; the skin friction is more influential. Figure 22 shows profiles near $(X/h)_c$ for pressure ratios of 2.8 and 3.6. The solid black curve is redrawn from Fig. 20. Thus, for a relatively short afterbody, the skin friction has not yet become dominant in Fig. 22, even at pressure ratio 2.8. Referring to Fig. 21, note that the profile at the same location $(X/h = 26.7)$ at pressure ratio 2.0 does, however, differ from the universal profile. Figure 23 shows profiles that are 40 fan heights further downstream than Fig. 22. This location is far enough downstream so that the profiles are dissimilar. Note that the profile at pressure ratio 3.6 is closer to the universal profile than the one at 2.8; also recall that the profile for $(P_t/P)_F = 4.4$ at the same location fell on the universal profile (Fig. 20).

The foregoing discussion is summarized in Fig. 24. All profiles whose location is to the left of the vertical curve line

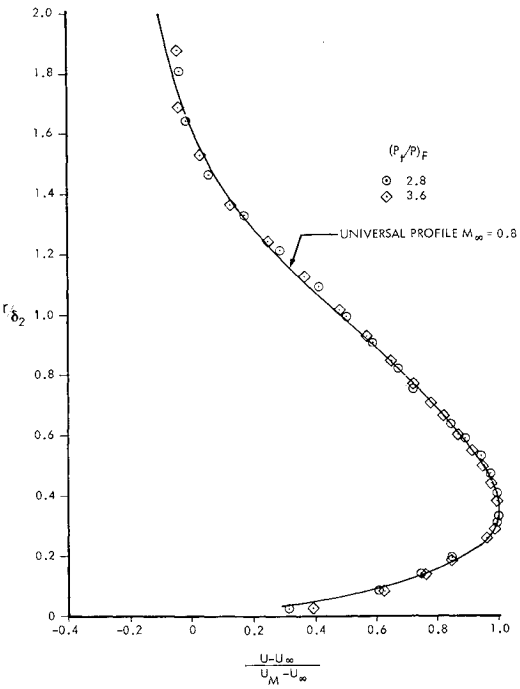

Fig. 22 Axisymmetric compressible wall jet velocity profiles: $M_\infty = 0.8$, $X/h = 26.7$, louvered turning sections, convergent nozzles.

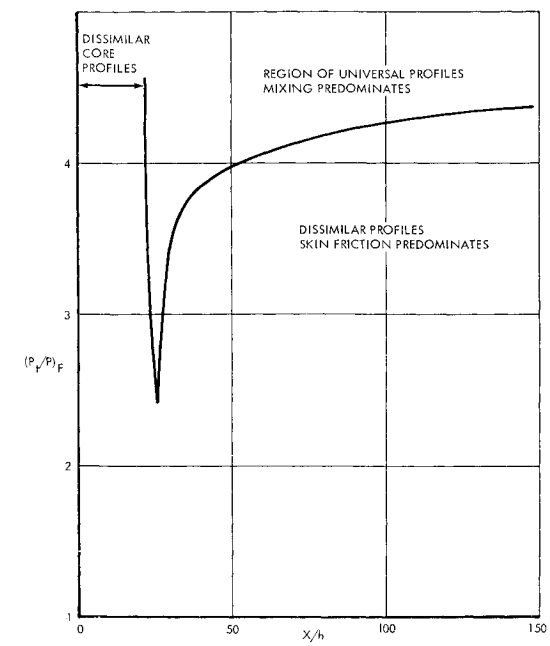

Fig. 24 Axisymmetric compressible wall jet (region of profile similarity): $M_\infty = 0.8$, louvered turning sections, convergent nozzles.

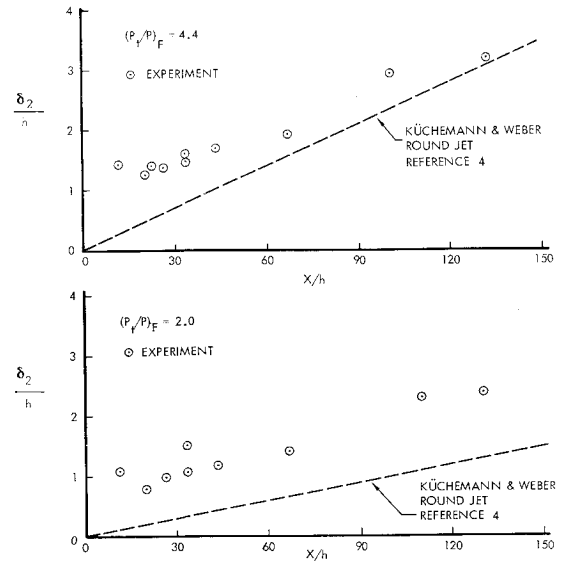

Fig. 25 Compressible wall jet spreading: $M_\infty = 0$, convergent nozzles, louvered turning sections.

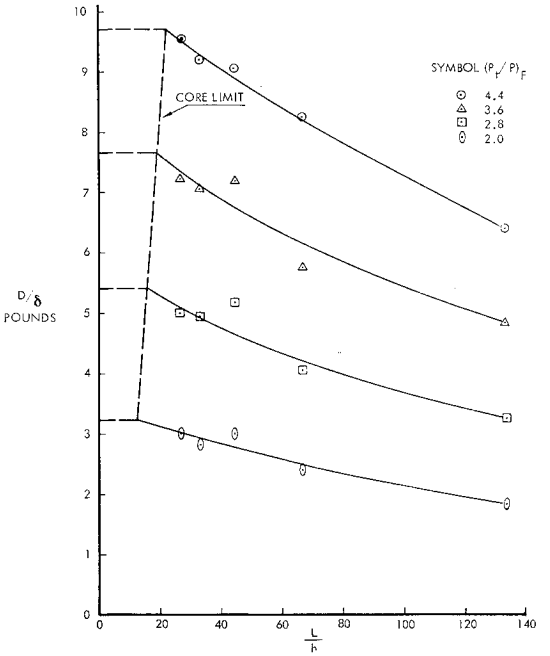

Fig. 26 Measured afterbody drag: $M_\infty = 0$, $L = 12$ in.

are influenced by the core region and consequently are not similar. All profiles located in the region marked dissimilar profiles (lower right) are dissimilar because $U_F \rightarrow U_\infty$, and X/h is sufficiently large so that the skin friction plays a larger part than the mixing. Finally, the region above the curved line and to the right of the vertical line is a region of profiles similar to the one shown in Fig. 20.

Jet Spreading

The spreading of the axisymmetric compressible wall jet from convergent nozzles when $M_\infty = 0.8$ is shown in Fig. 25. The data are scattered, and the spreading angles are very small, being about 1° at a pressure ratio of 4.4 and 0.6° at 2.0. Also shown are lines according to Küchemann and Weber[4] for round jets in freestream air.

VI. Afterbody Skin-Friction Drag Measurements

The skin-friction drag of the models was measured for the test conditions shown in Table 2. Each afterbody length was tested at every pressure ratio, fan height, and Mach number (120 test conditions in all). Figures 26–31 show the measured data in terms of afterbody skin-friction drag vs L/h. Instrumentation was calibrated to 1% accuracy, but the data show scatter of 5% at higher drag balance loads and up to 20% at lower loads.

The trend of the data in Figs. 26–28 may be explained by considering the variation of D/δ with L/h if L is held constant and h is increased from zero. When h is zero, the drag is zero, and L/h is infinite. If L is 12 in. and h is 0.9 in., L/h is 133, and D/δ is 6.4 lb at $(P_t/P)_F = 4.4$. As h is increased further, L/h decreases, and D/δ increases reaching $9\frac{1}{2}$ lb at $L/h = 26.7$. Data are not available for smaller L/h, but D/δ will continue to increase with h until the entire afterbody is submerged in the core region. Further increases in h will not change the average velocity over the afterbody, and the drag will remain constant while L/h decreases to zero.

The pressure measurements indicate that the core region has a downstream limit (core length), which is a function of $(P_t/P)_F$ and X/h. For instance, the core may extend to $X/h = 17$ or $X/h = 27.5$ for $(P_t/P)_F = 4.4$, and $M_\infty = 0$. Thus, the line drawn through the points for $(P_t/P)_F = 4.4$ may be extended to, say, $X/h = 22$ and then drawn at a constant value of D/δ to $L/h = 0$. In Fig. 26, the extended line would intersect the core ($X/h = 22$) at $D/\delta = 9.7$ lb, and D/δ would equal 9.7 lb for $X/h < 22$. Pressure measurement data may be used with the foregoing reasoning to estimate D/δ at small L/h for Figs. 26–31. The core limit line and the value of (D/δ) for small L/h are estimated and plotted as

Table 2 Test conditions for drag measurements

Afterbody length	Fan nozzle pressure ratio	Fan height, in.	Mach number
6	2.0	0.09	0
9	2.8	0.18	0.8
12	3.6	0.27	...
...	4.4	0.36	...
...	...	0.45	...

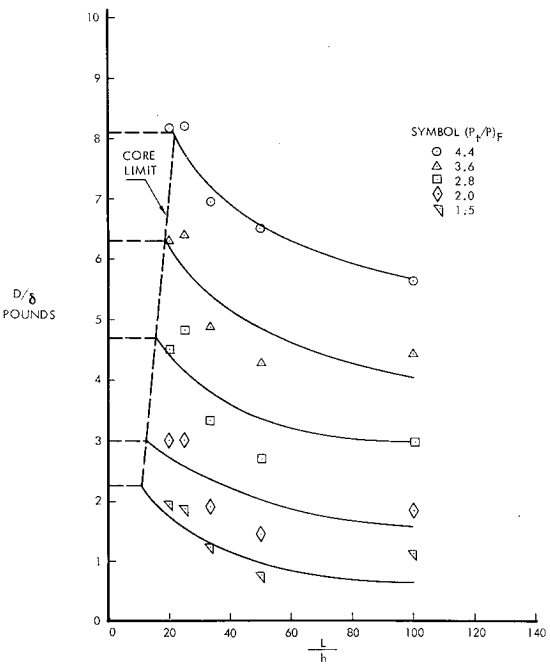

Fig. 27 Measured afterbody drag: $M_\infty = 0$, $L = 9$ in.

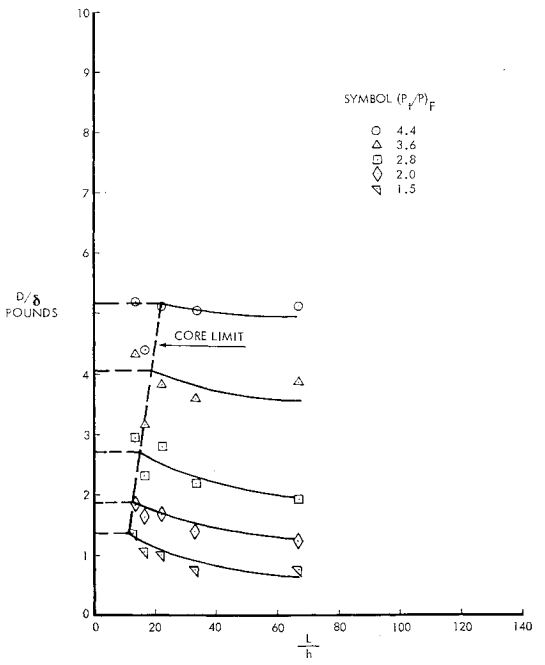

Fig. 28 Measured afterbody drag: $M_\infty = 0$, $L = 6$ in.

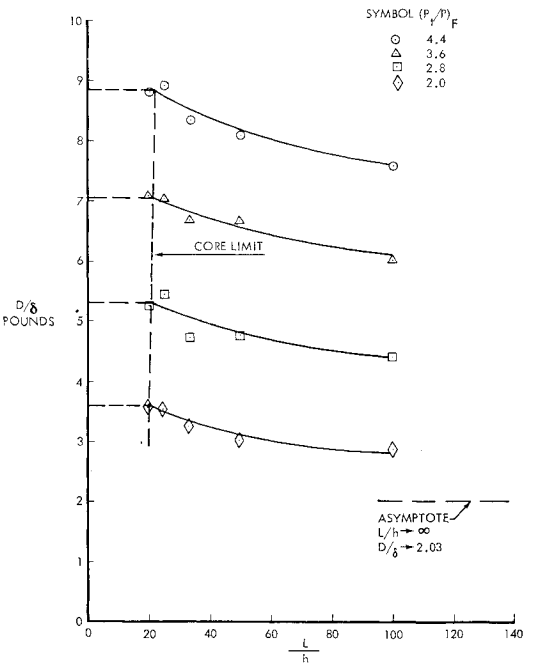

Fig. 30 Measured afterbody drag: $M_\infty = 0.8$, $L = 9$ in.

dashed lines on the figures. The accuracy of such extrapolations is, of course, limited by the assumptions about core lengths, which are strongly influenced by the internal geometry of the nozzle.

Figures 29–31 are for $M_\infty = 0.8$. The general behavior of the curves is similar to the curves for $M_\infty = 0$, except, when h goes to zero, a finite drag will exit due to the action of free-stream air over the afterbody. Thus as $L/h \rightarrow \infty$, D/δ will approach asymptotic values, and these are shown in Figs. 29–31.

Data from models with louvered and louverless turning sections were taken with the drag balance, but respective correlations were not found. When using the drag balance test results to predict full scale drag, it is recommended that R_F be used for scaling; the flow through the model and tunnel was at room total temperature, and the tunnel static pressure was about 9.6 psi. The reader is cautioned that conditions at full scale fan nozzle exits may differ markedly from model conditions.

VII. Velocity Decay: Skin-Friction Calculations

Before the drag tests, it was necessary to estimate the afterbody skin-friction drag, using boundary-layer theory. To do this, the local shear at the wall is related to the local maximum velocity in the boundary layer.

The skin friction in the core may be expressed as[9]

$$C_f = D/q_F A_w = 0.074(U_F X_c/\nu_F)^{-0.2} \qquad (6)$$

Downstream of the core, the maximum velocity decay is given

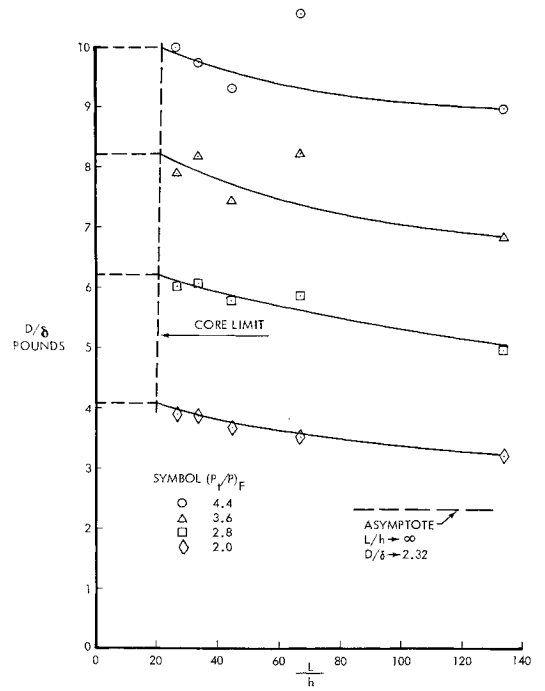

Fig. 29 Measured afterbody drag: $M_\infty = 0.8$, $L = 12$ in.

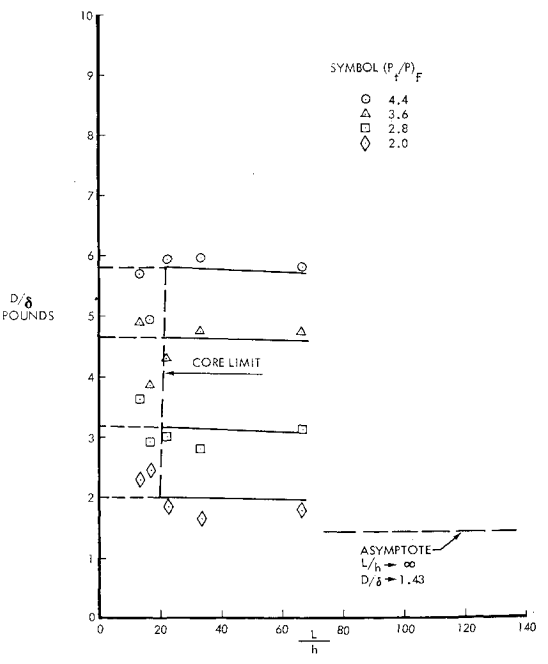

Fig. 31 Measured afterbody drag: $M_\infty = 0.8$, $L = 6$ in.

by

$$(U_M - U_\infty)/(U_F - U_\infty) = K(X/h)^B \quad (7)$$

where the value of K is found from the equation,

$$K(X/h)_c^B = 1.0 \quad (8)$$

The local shear stress is given by

$$\tau_w(X) = [1/(2\pi R_1)]dD/dX = \rho_F U_M^2(d\theta/dX) \quad (9)$$

where, for this calculation, ρ_F is assumed constant. According to the $\frac{1}{7}$ power law for turbulent boundary layers,

$$d\theta/dX = (\tfrac{7}{72})[d\delta(X)/dX] \quad (10)$$

and $\delta(X)$ is given by

$$(\tfrac{7}{72})[d\delta(X)/dX] = 0.0225[U_M\delta(X)/\nu_F]^{-1/4} \quad (11)$$

The initial condition for (11) is the value of $\delta(X)$ at X_c which is δ_c. This is found by integration of (11) with U_M equal to U_F. Equation (11) is then integrated between δ_c and $\delta(X)$ to get $\delta(X)$. When $\delta(X)$ is found, it is differentiated to get $d\delta(X)/dX$; this is substituted in (10) for $(d\theta/dX)$; $(d\theta/dX)$ is put in (9) to get $\tau_w(X)$; finally, $\tau_w(X)$ is integrated between X_c and L to get the drag downstream of X_c. The final result is

$$D = 2\pi R_1\rho_F\nu_F^{0.2}\left[0.036U_F^{1.8}X_c^{0.8} + 0.02883\int_{X_c}^{L} U_M^{1.75} \times \left\{\int_{X_c}^{X}(1/U_M^{0.25})dX + X_c/U_F^{0.25}\right\}^{-0.2}dX\right] \quad (12)$$

(The equation combines both the core and downstream regions.) It should be noted that the preceding analysis includes no compressibility correction; ρ_F and ν_F are taken at fully expanded fan nozzle exit conditions.

The core length and the decay constants for the louvered turning sections were used with Eq. (12) to calculate the drag of the 12-in. ($L = 12$) model at $M_\infty = 0.8$. The calculations are compared to experiment on a plot of D/δ vs Fg/δ in Fig. 32. At $(P_t/P)_F$ of 2.0 and 2.8, experimental results agree satisfactorily; however, at 3.6 and 4.4, the experimental drags are considerably higher. This is somewhat surprising, especially since the calculations in Eq. (12) are not corrected for compressibility, and intercept core lengths were used. The reason may be related to the wall jet turbulence. Hodgson[5] found that the flow downstream from a wall jet has a turbulence level much greater than the turbulence level found in boundary layers in wind tunnels. It was also noted that skin friction increases proportionately with the square root of the mean value of turbulent pressure fluctuations, and thus, wall jet skin-friction coefficients should be greater than flat-plate coefficients. This is particularly true with the apparatus of this test which required the flow to be turned 180° immediately upstream of the jet.

VIII. Conclusions

The skin-friction drag of short duct turbofan nacelle afterbody models has been measured for a variety of geometries, pressure ratios, and freestream Mach numbers, thus permitting the estimation of a major unknown component of nacelle drag. Boundary-layer skin-friction calculations show agreement for afterbody drag measurements at $(P_t/P)_F = 2.0$ and 2.8.

The decay of the velocity from a compressible axisymmetric wall jet is given by $U_M/U_F = K(X/h)^B$ when $M_\infty = 0$, and by $\phi = (U_M - U_\infty)/(U_F - U_\infty) = K(X/h)^B$ when $M_\infty = 0.8$. (Note that $U_M/U_F \equiv \phi$ when $U_\infty = 0$.) The constant B is -0.41 when $M_\infty = 0$, compared to -0.5 for the plane incompressible wall jet. When $M_\infty = 0.8$, B is a function of $(P_t/P)_F$. For $M_\infty = 0$ and $M_\infty = 0.8$, K is a function of $(P_t/P)_F$ and reflects the value of the core length. The core length differs with internal nozzle geometry.

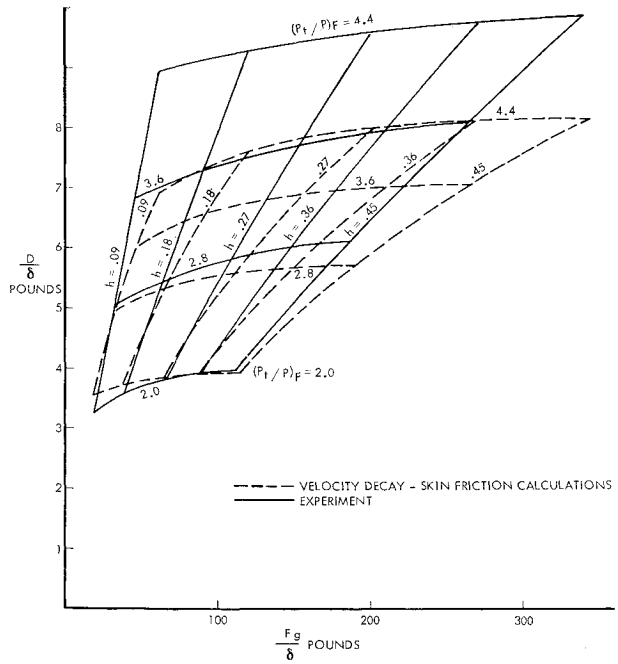

Fig. 32 Afterbody drag vs fan gross thrust: $M_\infty = 0.8$, $L = 12$ in.

When $M_\infty = 0$, the axisymmetric compressible wall jet velocity profiles are identical to Glauert's plane incompressible wall jet profile; compressibility (and to a limited extent axial symmetry) does not change the wall jet profile. When $M_\infty = 0.8$, a new universal velocity profile is found which differs from Glauert's profile, and which is applicable to limited geometries and flow conditions.

The velocity may be estimated downstream of the core when $M_\infty = 0$ by using Glauert's profile with the velocity decay and jet spreading data. It may also be estimated when $M_\infty = 0.8$, and $(P_t/P)_F$ and X/h lie in the universal profile region of Fig. 24.

References

[1] Lawrence, R. L., "Velocity profiles from compressible wall jets," AIAA J. **2**, 574 (1964).

[2] Schmieden, C. J. and Kawalki, K. H., "Contribution to the problem of flow at high speed," NACA TM 1233 (1949).

[3] Glauert, M. B., "The wall jet," J. Fluid Mech. **1**, Pt. 6, 625–643 (1956).

[4] Küchemann, D. and Weber, J., *Aerodynamics of Propulsion* (McGraw-Hill Book Co., Inc., New York, 1953), Chap. 10, pp. 235–239.

[5] Hodgson, T. H. and Lilley, G. M., "On surface pressure fluctuations in turbulent boundary layers," Boundary Layer Research Meeting, London, AGARD Rept. 276 (April 1960).

[6] Sigalla, A., "Experimental data on turbulent wall jets," Aircraft Eng. **30**, 131–134 (1958).

[7] Myers, G. E., Eustis, R. H., and Schauer, J. J., "Plane turbulent wall jet flow development and friction factor," American Society of Mechanical Engineers Paper 62-Hyd-4 (1958).

[8] Sigalla, A., "Measurements of skin friction in a plane turbulent wall jet," J. Roy. Aeronaut. Soc. **62**, 873–877 (1958).

[9] Schlichting, H., *Boundary Layer Theory* (McGraw-Hill Book Co., Inc., New York, 1960), 4th ed., Chap. XXI, p. 537, Eq. (21.11).

[10] Shapiro, A., *The Dynamics and Thermodynamics of Compressible Fluid Flow* (Ronald Press Co., New York, 1953).